

Temperature-Responsive Multistable Metamaterials

Lucia M. Korpas,[†] Rui Yin,[†] Hiromi Yasuda, and Jordan R. Raney*Cite This: *ACS Appl. Mater. Interfaces* 2021, 13, 31163–31170

Read Online

ACCESS |



Metrics & More



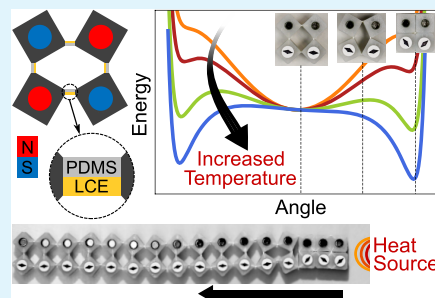
Article Recommendations



Supporting Information

ABSTRACT: The ability for materials to adapt their shape and mechanical properties to the local environment is useful in a variety of applications, from soft robots to deployable structures. In this work, we integrate liquid crystal elastomers (LCEs) with multistable structures to allow autonomous reconfiguration in response to local changes in temperature. LCEs are incorporated in a kirigami-inspired system in which squares are connected at their vertices by small hinges composed of LCE–silicone bilayers. These bend and soften as the temperature increases above room temperature. By choosing geometric parameters for the hinges such that bifurcation points in the stability exist, a transition from mono- or tristability to bistability can be triggered by a sufficient increase in temperature, forcing rearrangements of the structure as minima in the energy landscape are removed. We demonstrate temperature-induced propagation of transition waves, enabling local structural changes to autonomously propagate and affect other parts of the structure. These effects could be harnessed in applications in interface control, reconfigurable structures, and soft robotics.

KEYWORDS: 3D printing, mechanical metamaterials, liquid crystal elastomers, stimulus responsive, soft active materials



■ INTRODUCTION

The ability to change shape and function is an essential behavior of many mechanical systems, e.g., for deployable structures,^{1–4} tunable wave propagation,^{5–7} adaptive locomotion,⁸ and autonomous robotic systems.^{9,10} One strategy for rapid structural reconfiguration that has been explored extensively in recent years is to use multistable mechanisms, which support multiple stable configurations. By harnessing the transition between these discrete states, multistable systems have been used to demonstrate complex responses to simple mechanical loads, such as dynamic reconfiguration^{11–13} and mechanical memory and logic.^{14–17} These exciting properties, particularly the ability to store and process simple information, raise the question of how mechanical metamaterials can be employed in applications in which some degree of programmable, autonomous responsiveness is required. Can mechanical systems sense, compute with, and actuate in response to both mechanical and nonmechanical changes in their environment, for example, to regulate the behavior of deployable structures and soft robots?

Continued advances in the development of stimuli-responsive materials, which deform upon exposure to heat, light, or other nonmechanical signals, provide an opportunity to program actuation, function, and information state in direct reaction to environmental cues.^{18–20} Liquid crystal elastomers (LCEs) in particular have received much recent attention for their ability to change shape in response to temperature and their programmability through 3D printing.^{21–24} While LCEs and other stimuli-responsive materials can serve as actuators on their own, the time and length scales of the actuation are often limited by diffusion, fabrication constraints, and poor

mechanical properties. Some of these challenges can be mitigated by enhancing the action of stimuli-responsive materials via structural instability,^{21,25,26} e.g., via the inclusion of other materials as constraining features.^{27–29} A multistable architecture can be combined with stimuli-responsive materials to speed up, amplify, or discretize shape change, which has enabled reconfigurability, locomotion, and binary logic in response to environmental signals.^{30–34} However, the introduction of active materials into multistable architectures creates many problems when designing reconfigurable mechanical systems. Even without stimuli-responsive materials, multistable mechanical metamaterials already exhibit complex nonlinear mechanical behaviors such as instabilities and bifurcations. The addition of stimuli-responsive materials, which can undergo large changes to their mechanical properties (e.g., stiffness) in response to changes in their environment, further complicates the process of designing controllable reconfigurability in these systems.

In this work, we therefore introduce design phase diagrams that help account for both the nonlinear mechanical response of multistable architectures and the time dependence of the stimuli-responsive materials of which they are composed. Here, we use a multistable architecture based on the assembly of rotating squares (Figure 1), a system capable of dynamic

Received: April 21, 2021

Accepted: June 11, 2021

Published: June 24, 2021



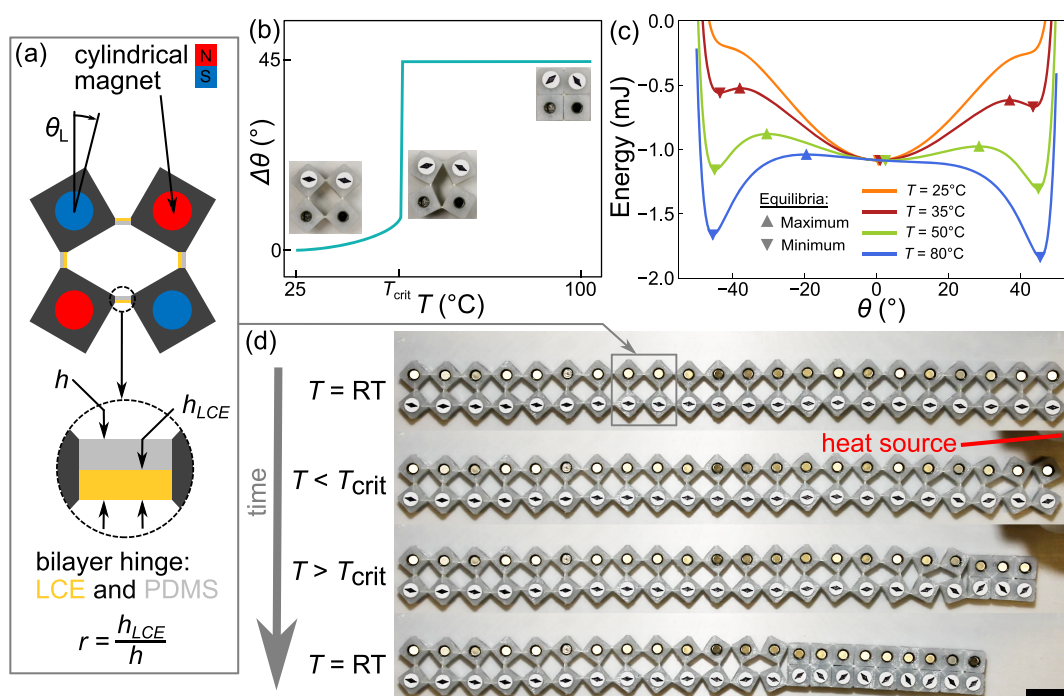


Figure 1. Multistable temperature-responsive metamaterial concept. (a) Schematic of a representative portion of the metamaterial, showing squares with embedded cylindrical magnets and PDMS-LCE bilayer hinges connecting adjacent vertices. For a fixed lattice spacing and magnetic moment, the metamaterial behavior can be defined by geometric parameters: the total hinge thickness h , the proportion of the hinge that is temperature responsive LCE $r = h_{LCE}/h$, and the initial folding angle θ_L . (b) As the temperature is increased, the LCE contraction and softening causes the squares to rotate, as shown here schematically. The resulting change in the angle is continuous until the bifurcation point at T_{crit} where the structure becomes unstable and rapidly snaps to the nearest stable configuration. (c) Modeled energy landscape for one unit of the structure (i.e., the four squares in panel (a)) is given (a function of h , r , and θ_L), corresponding to a structure that is monostable at room temperature (orange). Increasing the temperature softens the hinges enough that the strength of the magnets produces new stable configurations near $\pm 42^\circ$ (green); further temperature increase eliminates the original stable configuration (blue). (d) This phase transformation allows a chain of this material, originally at room temperature (RT), to move away from a localized heat source if a temperature threshold is temporarily exceeded. The scale bar is 20 mm.

reconfiguration and propagation of transition waves.¹² We couple this architecture with temperature-responsive LCEs to locally vary the mechanical properties and shape of the metamaterial. By doing so, we demonstrate that the environmental sensing input is directly converted into spatially and temporally varying control over the metamaterial configuration. Further, we demonstrate a practical design strategy for achieving targeted autonomous behaviors, i.e., particular structural reconfigurations in response to elevated temperatures.

To start, we employ a multistable mechanical metamaterial based on the rotating squares mechanism, which has been characterized previously,¹² but here add LCEs in composite hinges that cause internal rotations in response to temperature changes. As shown in prior work, the rotating squares mechanism is able to support multiple stable configurations by embedding magnets within the squares.^{12,35–37} Interestingly, a transition of states in one location can, depending on the energy landscape, propagate through the structure causing global shape change. In this work, the temperature responsiveness of the hinges allows these shape changes to take place autonomously in response to the environment. The hinges consist of two layers—a silicone, poly(dimethylsiloxane) (PDMS), and a temperature-responsive LCE—which are individually 3D printed, joined via a silicone sealant, and inserted into grooves molded into the squares (Figure 1). The hinges are characterized by two parameters:

the total hinge thickness h and the ratio of the LCE thickness h_{LCE} to the total thickness of the hinge $r = h_{LCE}/h$ (Figure 1a). A third parameter, the initial folding angle θ_L of the squares, is also prescribed; this is set to zero for the experiments in this work due to fabrication constraints. The magnets are placed with alternating polarity such that the magnets in adjacent squares attract one another. At a given temperature, the number of stable configurations of the metamaterial unit is determined by the three parameters described above. As the temperature is increased, the LCE contracts and softens relative to the PDMS, causing the bilayer hinges to bend and the squares to rotate by a change in angle $\Delta\theta$ from the equilibrium room-temperature position (Figure 1b). This corresponds to a dramatic shift in the energy landscape of the hinges as a function of the total rotational angle θ , as shown in Figure 1c. At 25 °C, there is a single-energy minimum at $\theta = 0$ (orange curve in Figure 1c). Increasing the temperature to 50 °C softens the hinges; this results in the appearance of local minima near $\theta = \pm 42^\circ$ due to magnet–magnet interactions, making the system tristable (green curve in Figure 1c). The temperature-induced bending of the hinges also results in the local minimum originally at $\theta = 0$ to shift rightward. As the temperature increases from 50 to 80 °C (the green and blue curves in Figure 1c, respectively), the energy barrier separating the new local minimum near $\theta = 42^\circ$ from the original minimum decreases until it is reduced to zero at a critical temperature T_{crit} . This defines a bifurcation point as the

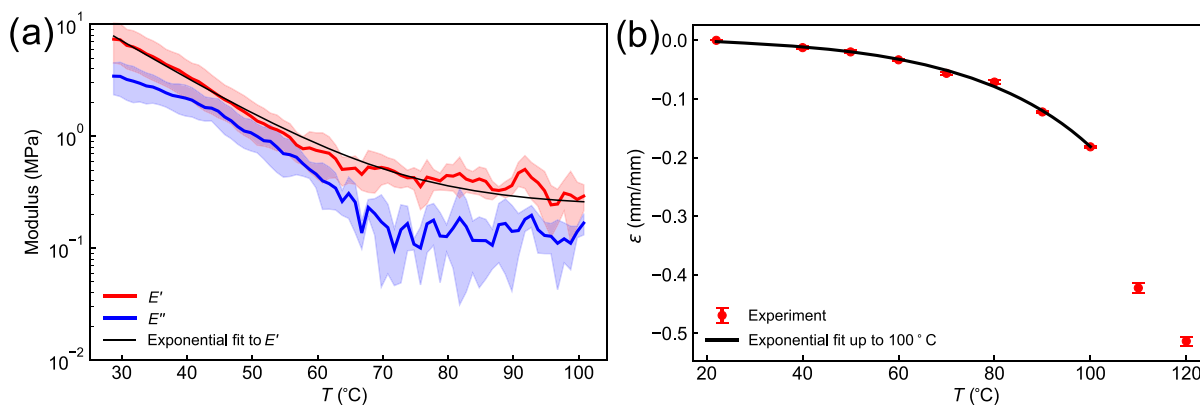


Figure 2. Mechanical properties of the 3D printed liquid crystal elastomer (LCE). (a) Tensile storage modulus E' and loss modulus E'' decrease by more than an order of magnitude upon heating. An exponential function is empirically fit to the former ($R^2 = 0.995$) to allow this material temperature dependence to be easily included in the design phase diagrams for the metamaterial, discussed later. (b) LCE contracts along the director orientation upon heating; an exponential function is again empirically fit (up to a temperature of 100 °C) so the temperature response of the material can be easily accounted for in the metamaterial design phase diagrams ($R^2 = 0.996$).

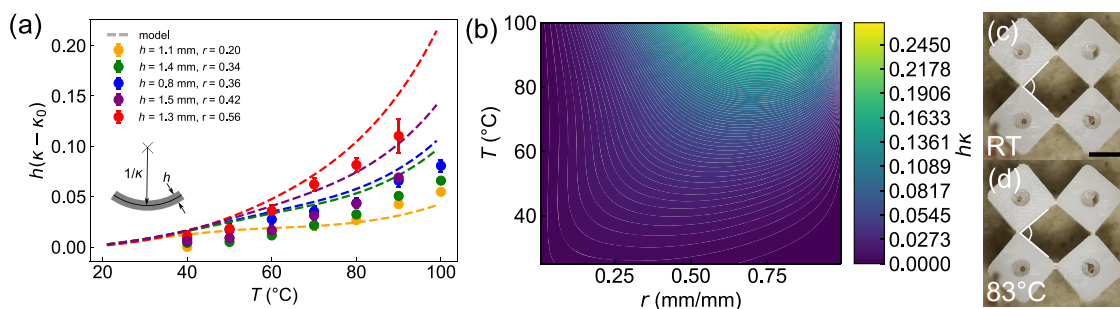


Figure 3. Bilayer hinge curvature and metamaterial bending angles. (a) Normalized curvature $h(\kappa - \kappa_0)$ of PDMS-LCE bilayer strips, with curvature κ_0 at room temperature, is measured and compared with the curvature predicted by the modified Timoshenko bilayer model for a range of h and r values. (b) Normalized curvature generally increases with temperature and is maximized for $r = 0.75$. (c, d) Metamaterial unit with $(h, r, \theta_L) = (1.08 \text{ mm}, 0.37, 0)$, without magnets, showing the angle between squares (c) at room temperature (88.5°, corresponding to $\theta_T = 0.75^\circ$) and (d) at elevated temperature (79.9°, corresponding to $\theta_T = 5.05^\circ$). The scale bar is 10 mm.

system moves from tristability to bistability. Assuming that the system begins in the original stable configuration near $\theta = 0$, once the temperature passes through this bifurcation point (and the original stable configuration is therefore lost), the unit quickly actuates by snapping to the nearest remaining stable point, near $\theta = 42^\circ$ (blue curve in Figure 1c). This is represented by the abrupt, large-magnitude change in $\Delta\theta$ at T_{crit} as shown in Figure 1b. (Note that while the hinge bending energy is always zero or positive, the net energy is negative as a result of the magnetic attraction.) The value of T_{crit} is dependent on (h, r, θ_L) . Because this transformation occurs as a result of local property changes at the hinges, applying heat to only a portion of a chain will result in a localized change in stability (Figure 1d).

RESULTS AND DISCUSSION

Characterization of Bilayer Hinges. To quantitatively predict the dependence of the hinge angle and stiffness on temperature, we first characterize the temperature-dependent material properties of the LCE and PDMS individually. The temperature response of the bilayer hinge is defined by the distinct effects of temperature on the two individual materials, including relative changes to strain and distinct temperature dependence of the elastic moduli. During extrusion, the LCE director aligns along the print direction as a result of the shear stress in the nozzle^{21,22} (Figure S3), producing anisotropic

stiffness and temperature response of the LCEs. After curing, the LCE elastic storage modulus $E'(t)$ along the direction of director orientation decreases with increasing temperature, dropping roughly an order of magnitude between room temperature and 100 °C (Figure 2a). As the temperature is increased from room temperature up to the nematic-to-isotropic transition point of the LCE (85 °C), the LCE contracts along the direction of alignment, reaching a strain of around $\epsilon = 0.2$ at 100 °C (Figure 2b). In contrast, for PDMS, the stiffness and strain do not change significantly with temperature over this temperature range (Figure S5).

The temperature-dependent mechanical properties of the LCEs provide a predictable temperature dependence to the bilayer hinges, which change the energy landscape of the metamaterial. The observed temperature dependence of the metamaterial depends on the geometric parameters defining the hinges (h, r). We therefore model the relationship between the hinge curvature and stiffness and the geometric parameters (subsequently validated by experimental prototypes). The temperature-induced contraction and softening of the LCE results in bending about an axis perpendicular to the LCE print path, with curvature $\kappa(T)$.^{38–40} To model κ as a function of the geometric and material parameters, we modify the Timoshenko bilayer strip model^{38,39,41} by incorporating the experimental data for the temperature dependence of the strain $\epsilon(T)$ and storage modulus $E'(T)$, each of which we

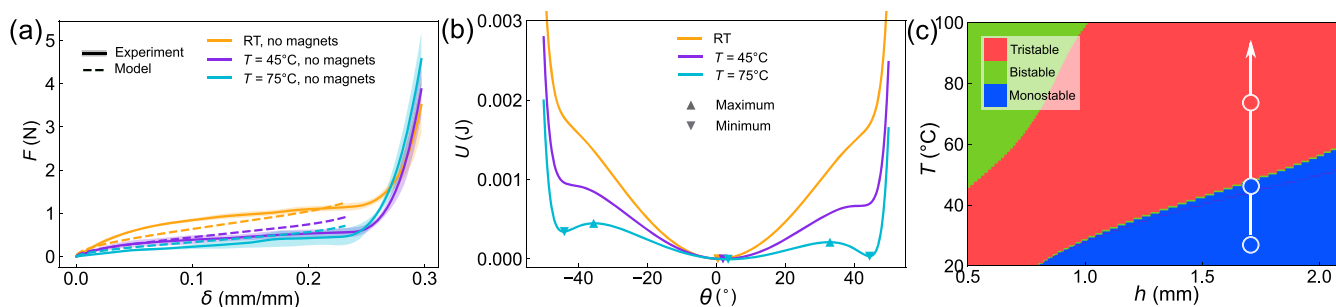


Figure 4. Metamaterial stiffness and phase change upon heating. (a) Load–displacement experiments for units without magnets, showing stiffness decreasing with temperature as the LCE softens, for $(h, r, \theta_L) = (1.71 \text{ mm}, 0.18, 0)$ at room temperature (red), 45 °C (green), and 75 °C (blue). The solid lines and surrounding shaded area correspond to the experimentally measured mean and standard deviation, respectively, and the dotted lines to the model. (b) Energy landscapes obtained from the models calibrated in panel (a) after adding magnets. As the temperature is increased, the LCE softens and contracts, resulting in the appearance of two additional energy wells for $T = 75 \text{ °C}$ and in the rightward shift of the center energy well. (c) Phase diagram for $r = 0.18$ and $\theta_L = 0^\circ$, showing the location of the experimental values for stability (shaded circles) within the modeled h – T phase space (shaded regions). The temperature of transition from the monostable phase to the tristable phase increases with h .

empirically approximate as exponential functions (see the SI for the derivation of the model). Despite its simplicity, this model captures the bending behavior, as shown by the general agreement with experiments for five different (h, r) parameter combinations (Figure 3a). In particular, the normalized curvature $h\kappa$ increases with r . The model predicts that $h\kappa$ should be independent of h , which we find to be a reasonable assumption for our composites (see Figure S7). Given this, we model the dependence of $h\kappa$ over $r \in [0, 1)$ for temperatures up to 100 °C. Within this temperature range, the maximum achievable curvature is reached at $r = 0.75$, above which the decrease in the LCE's elastic modulus relative to that of the PDMS prevents further curvature increase (Figure 3b).

Metamaterial Multistability and Temperature Dependence. After quantifying the temperature dependence of the hinges as described above, we fabricated mechanical metamaterials with these hinges to provide deterministic parameter changes in response to temperature changes. Bilayer hinges of width $w = 10 \text{ mm}$ were added by hand to premolded silicone squares, such that the print direction of the LCEs in the hinge lies along the arc length of the hinge. The arc length s relates κ to the temperature-dependent change in the angle as $\theta_T(T) = \kappa(T)s$. Figure 3c,d shows an example of a change in θ_T of 4.3° occurring with a temperature increase. Fabrication tolerances introduce some error in prescribing a nominal arc length proportional to h . We therefore use an empirical model to establish a relationship between h and the effective arc length (see Figure S8), which provides a good prediction of θ_T for our experimentally tested values.

If there are no magnets at the centers of the squares, the metamaterial has its lowest-energy configuration at $\theta_0(T) = \theta_L + \theta_T(T)$, and the strain energy of the hinges increases monotonically if displaced from this equilibrium. We model this strain energy with an effective torsional stiffness of the hinge $k(T)$, which defines the hinge deformation energy $U_H(\theta, T)$, with $\theta = \Delta\theta + \theta_0$. Additionally, a strain energy term $U_{\text{limit}}(\theta)$ is included, corresponding to the compression of the squares when the faces of adjacent squares come into contact. We model this collision empirically as a pair of nonlinear springs with zero magnitudes when $\theta = 0$. The magnetic contribution $U_M(\theta)$ is accounted for by modeling the magnets as point dipoles of magnetic moment m at the centers of the adjacent squares with alternating polarity, such that adjacent magnets attract (this is restricted to nearest-neighbor pairwise

interactions for simplicity). Thus, the total strain energy for a pair of squares is defined by

$$U(\theta, T) = U_H(\theta, T) + U_M(\theta) + U_{\text{limit}}(\theta) \quad (1)$$

(see the SI for the derivation). When the distance d between the centers of adjacent squares is prescribed, the force F required to hold the metamaterial at a strain $\delta = (d - a)/a$ with equilibrium lattice spacing a can be derived from $U(\theta, T)$ (see the SI).

Figure 4a shows the experimentally observed and modeled load–displacement relation for $(h, r, \theta_L) = (1.71 \text{ mm}, 0.18, 0)$, demonstrating that as the temperature is increased, the reduction in LCE stiffness E_{LCE} lowers the spring constant from $k = 7.0 \text{ mNm}$ at 25 °C to $k = 2.4 \text{ mNm}$ at 75 °C. Once the model parameters are determined as in Figure 4a, we can add the magnet potential $U_M(\theta)$ to model the corresponding energy landscapes, as shown in Figure 4b. We find that the predicted stability is in reasonable agreement with the experimentally observed behavior for the units with magnets, as shown in Figure S9. In this example, the spring energy U_H dominates at room temperature, resulting in monostability (red curve in Figure 4b, stable only near $\theta = 0$). If we increase the temperature T , which leads to the decrease in k , the change in θ_T resulting from the LCE contraction introduces asymmetry to the energy landscape (green curve in Figure 4b). If the temperature reaches 75 °C, the structure forms two additional local minima (blue curve in Figure 4b), i.e., tristability.

Multistability Phase Boundary Analysis. Using the energy model, we can not only map the stability of a given parameter combination across temperatures but also find the locations of the boundaries between stability regimes for a range of parameter values. In Figure 4c, we show the locations of the mono- (blue), bi- (green), and tristable (red) regions for $h = [0.5, 2.5] \text{ mm}$ and $(r, \theta_L) = (0.18, 0)$ and plot the experimental measurements with shaded circles. In this case, we find that a transition from the monostable to the tristable region occurs around $T = 47 \text{ °C}$. (A narrow band of bistability appears around $\theta = +42^\circ$, before the one at $\theta = -42^\circ$, due to the asymmetry of the energy landscape.) This ability to predict the critical temperatures at which the phase boundaries will be crossed enables the design of systems that undergo a qualitative change in behavior at prescribed temperatures. By carefully choosing the fabrication parameters of the meta-

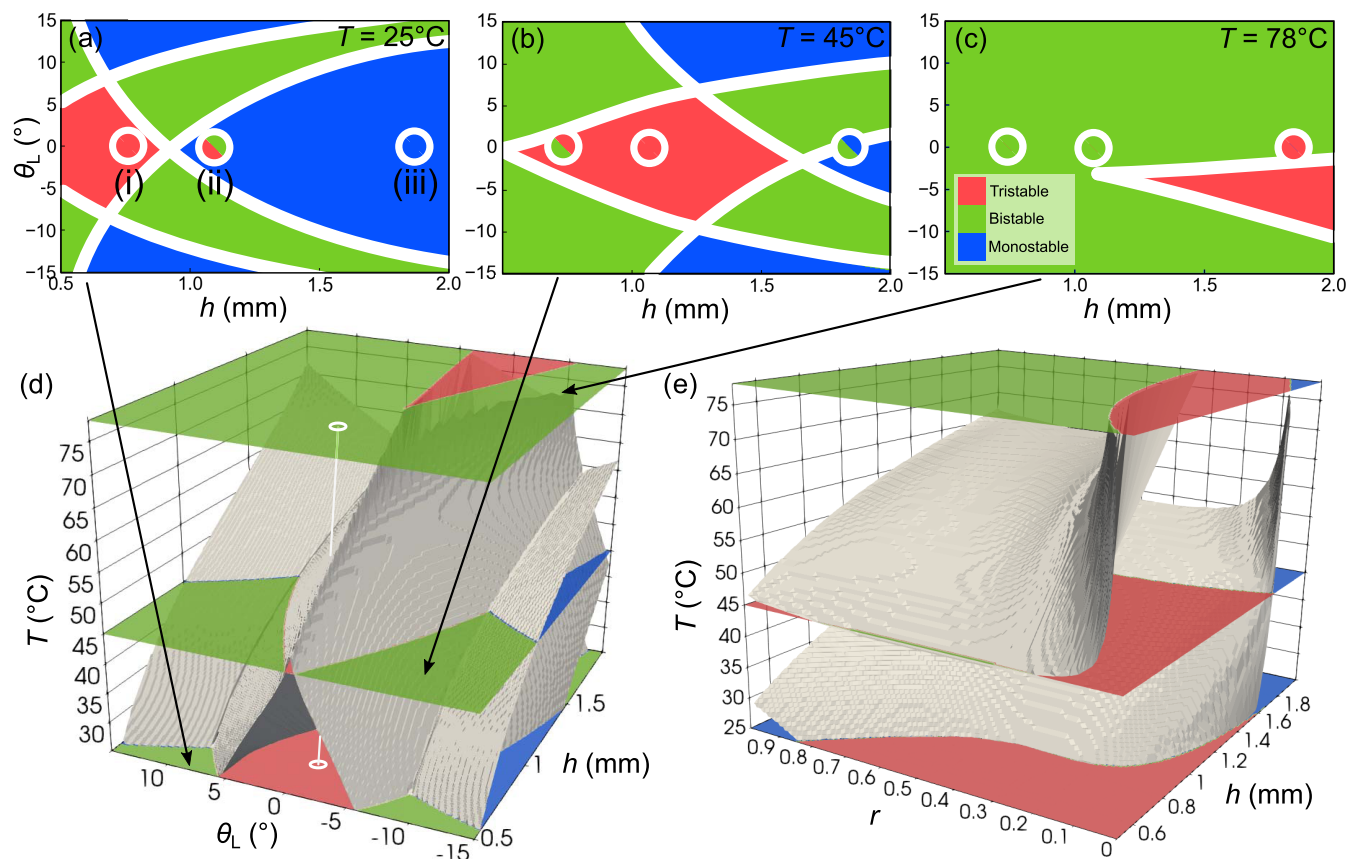


Figure 5. Effect of geometric parameters and temperature on stability. (a–c) Phase diagrams showing regions of mono-, bi-, and tristability (blue, green, and red, respectively) shifting as the temperature increases from (a) 25°C to (b) 45°C to (c) 78°C . The white lines indicate the boundaries between phase regions, with some nonzero thickness to indicate uncertainty in the model arising from uncertainty in the experiments used to calibrate it. The experimental results are shown as circles, with the infill color corresponding to the stability determined experimentally; a split infill is used to denote uncertainty in the stability due to the viscoelasticity of the materials, which is not accounted for in the model. (d) Phase diagrams in (a–c) are isotherms in a 3D phase space, shown intersecting the phase boundary surfaces (white); in this case with $r = 0.37$ held constant. The white vertical line shows how (i) (see panel (a)) passes through the boundary surface separating tristability and bistability. (e) Similar phase diagram but now showing the effect of r , with $\theta_L = 0$ fixed.

material, we can choose where the phase boundaries will be located and at what temperatures they will be crossed. For the specific r value in Figure 4c, this temperature varies as a function of h by more than 50°C ; with an appropriate choice of r , this boundary can be set arbitrarily close to room temperature within our fabrication range.

The phase boundaries can be controlled via several parameters. Figure 5 shows how h , θ_L , T , and r influence the phase boundaries. We perform quasi-static displacement tests of samples with (i) $h = 0.74$ mm, (ii) $h = 1.08$ mm, and (iii) $h = 1.81$ mm, holding fixed $\theta_L = 0$ and $r = 0.37$. The experimentally observed stability of these samples at $T = 25$, 45 , and 78°C is shown by the fill color of the circles in Figure 5a–c. At room temperature, (i) and (ii) are tristable, while (iii) is monostable (Figure 5a). At 45°C , (i) has become bistable (Figure 5b), and at 78°C , (ii) has become bistable and (iii) has become tristable (Figure 5c). The locations of the boundaries between the stability regions in h – θ_L phase space will shift with temperature due to the change in $k(T)$ and $\theta_T(T)$. To determine the locations of these boundaries based on the experiments, we find the correspondence between arc length and hinge thickness, which allows the phase diagram to best represent the stability of the samples. Because the model assumes rigidity of the squares in axial compression, we also find the magnetic moment that allows us to compensate for the

compression of the hinges and squares when the magnets are inserted. The resulting stability regimes at each temperature are shown by the colored regions in Figure 5a–c, with the phase boundaries denoted by thick white lines to indicate experimental uncertainty.

The boundaries in each of the three h – θ_L phase diagrams represent isotherms in phase space. Sweeping over temperature, these curves form surfaces in the three-dimensional phase space defined by h , θ_L , and T . We plot the resulting boundary surfaces in Figure 5d, representing these in gray and showing the intersection of these with the isotherms defined in Figure 5a–c. This three-dimensional phase diagram allows the selection of fabrication parameters according to the desired sequence of phase transformations. Note that while we experimentally demonstrate only samples with $\theta_L = 0$ due to fabrication constraints, the inclusion of θ_L as a fabrication parameter allows a richer design of the phase transformation behavior. For the case of $\theta_L = 0$, we can observe how the locations of the phase boundaries will shift with r . We plot the resulting boundary surfaces and corresponding isotherms in Figure 5e using the best-fit values from the previous analysis. In this plot, the phase boundary surface separating the tristable (red) and bistable (green) regimes corresponds to the surface of bifurcation points T_{crit} . By fixing one of the three design parameters (h , r , θ_L), such a three-dimensional phase diagram

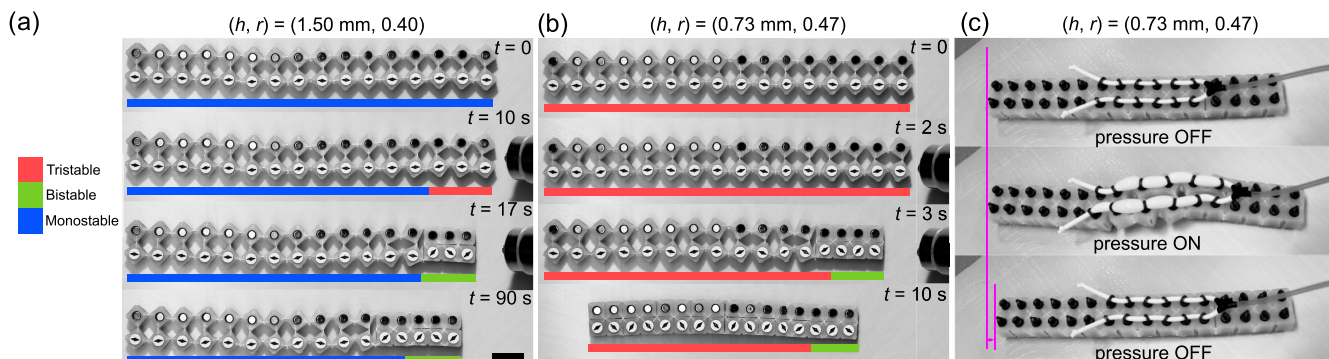


Figure 6. Actuation of 1D systems using temperature and pressure. (a, b) Homogeneous chains start in the open phase, with (a) $(h, r) = (1.50 \text{ mm}, 0.40)$ and (b) $(h, r) = (0.73 \text{ mm}, 0.47)$. The chains are exposed to a high temperature (around $100 \text{ }^\circ\text{C}$, well above T_{crit}) immediately after $t = 0$ and localized at a few units on the right end of the chain. These units rotate as T approaches T_{crit} for the transition to bistability. The scale bar is 20 mm . In (a), most of the chain remains monostable, hence the transition does not propagate; in (b), the transition propagates since most units are tristable. (c) Locomotion can in principle be enabled by pneumatically actuating a section of a tristable chain (here, “feet” have been added under the substrate to facilitate movement).

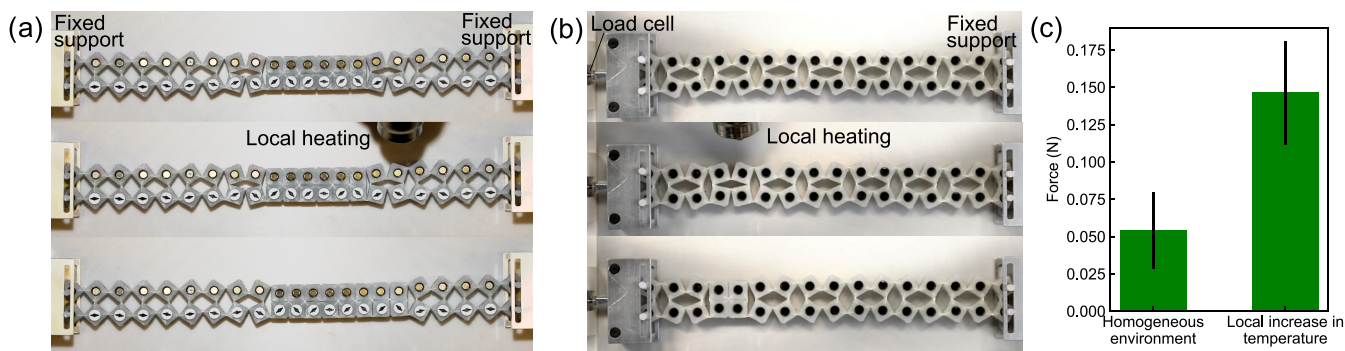


Figure 7. Demonstration of distributed sensing by a fixed-length chain. (a) For a starting configuration of a tristable chain, which includes both open and closed phases, only local heating at the phase boundaries, rather than in the bulk of a phase, will be recorded by a local change in the phase. (b) For a homogeneous starting configuration of a monostable chain, local heating can be recorded by a phase transformation near the point of application. Due to the LCE viscoelasticity, the phase change persists after the material cools but can be reversed by resetting the chain to its maximum length. (c) Force readout from a load cell connected to the left end of the chain in (b), corresponding to the external force required to keep the chain in the configuration shown. A higher force is read when the chain has sensed a high temperature.

can be used to select the remaining two parameters to prescribe T_{crit} and therefore the actuation temperature.

Actuation and Nonlocal Response. The individual units can be linked into longer chains to form a mechanical metamaterial that can interact with, respond to, and move through its environment (Figure 6). The temperature response of these metamaterials has both a temporal component (e.g., a function of heat diffusion) and a spatial component (e.g., different units in the chain can have different temperatures from one another). Moreover, since the units are mechanically coupled, changes to one can propagate to others, introducing temporal and spatial effects related to the nonlinear dynamics of the body. Harnessing these temporal and spatial components could allow the construction of soft structures that autonomously respond to their environment. To explore these ideas, we build two chains, one with $(h, r) = (1.50 \text{ mm}, 0.40)$ and the other with $(h, r) = (0.73 \text{ mm}, 0.47)$. These are experimentally observed to be monostable and tristable, respectively, which is in agreement with the stability predicted by the model (Figure S10). Starting from the open state, uniformly raising the temperature of each chain would eventually result in a transition to the closed state, though at different times. However, when heating is applied locally to the chain (for example, at one end) the long-term behavior of the

two chains is very different. The first instance is shown in Figure 6a and SI, Video 1. Even though the right end transitions to the closed state, the rest of the chain will remain open even after the temperature has exceeded T_{crit} because the bulk of the chain remains monostable. On the other hand, when the bulk of the chain is tristable, it can propagate a transition wave when one or both closed states are lower energy than the open state,¹² causing global structural reconfiguration despite the local nature of the stimulus. In this case, heating only a few hinges on one end of the chain will trigger the closing of the entire chain, as shown in Figure 6b and SI, Video 2. The result of this global response to a local stimulus can be harnessed to enable locomotion above a critical temperature. For example, by the addition of a pneumatic actuator, a tristable crawler can actuate by partially reopening the squares, such that it can only move once the closing of the squares has been triggered either by a transition wave or by global heating (demonstrated in Figure 6c and SI, Video 3; see Section 3 and Figure S2 for details on the crawling mechanism). This effect could be leveraged in soft robotics, for example, to enable a robot to behave differently depending on its environment, changing behaviors autonomously without external commands.

Reconfigurable Boundaries between Metamaterial Phases. The above properties of the chain can also be used to produce a distributed sensor by constraining the ends of the chains. Chains of different parameters can remain at rest in a variety of phase combinations even at room temperature when holding fixed the distance between endpoints. For this demonstration, the same two chains that are described in Figure 6 are used. Many local minima exist in the overall chain configuration for the tristable chain, separated by the localized multistable potentials as well as by friction (see the SI for efforts to mitigate friction). Beginning with one such configuration, shown in the top panel of Figure 7a, a heat source is applied to the hinges at a boundary between a closed phase and an open phase (middle panel). After T_{crit} is surpassed locally at the point of application of heat, the unit at the boundary closes, expanding the closed phase toward the right (bottom panel). The implications of this local phase change on the overall chain behavior are further demonstrated in a monostable chain in Figure 7b,c. Here, a load cell is attached to the left end of a chain and a fixture to the right end, such that the left- and rightmost squares can rotate but not horizontally translate. Under these constraints, the configuration with the lowest energy at room temperature is a homogeneous open phase due to the monostability of the chain. When heat is applied locally to the center of the chain, a single unit collapses to the closed phase (Figure 7b). This necessarily increases the force in the chain (Figure 7c). The chain retains this configuration after it cools due to the viscoelasticity of the material, preserving the history of the environmental signal. By embodying localized environmental inputs in the transition of individual units, the system discretizes the inputs such that changes in the state can be reliably measured from elsewhere along the chain, a prerequisite for digital logic. Thus, temperature-induced transformations enable actuation and memory in response to the system's environment, which, together with the intrinsic nonlinear dynamics of these systems,^{11–13,17} could allow one additional mechanism for autonomous behaviors in soft robotic systems.

CONCLUSIONS

In summary, we introduce a temperature-responsive multistable metamaterial and characterize the dependence of its stability on the geometric parameters and on the temperature. A linear-elastic bilayer model of the hinge deformation, with LCE contraction modeled by a temperature-dependent thermal expansion coefficient, is found to be sufficient to quantitatively capture the decrease in stiffness and increase in the bending angle of the PDMS-LCE hinges. We show that this change in hinge properties alters the energy landscape of the metamaterial unit, enabling phase transitions between stable configurations. These regimes of stability are represented in 2D and 3D phase diagrams and validated experimentally; these diagrams show the location of the boundary lines/surfaces between phases, and, therefore, the bifurcation point T_{crit} at which this transition will cause actuation for a given parameter combination. They could therefore be helpful tools for designing stimuli-responsive metamaterials with target autonomous, dynamic responses. A local increase in heat can trigger local and/or global reconfigurations of the chain, depending on the choice of parameters; these effects could be harnessed to enable autonomous actuation and adaptation to the environment,

e.g., for applications in soft robotics. Moreover, since the bifurcation-based mechanism is also scale-independent, these autonomous changes could in principle be miniaturized, e.g., for microscale or medical robotics.

ASSOCIATED CONTENT

Supporting Information

The Supporting Information is available free of charge at <https://pubs.acs.org/doi/10.1021/acsami.1c07327>.

Actuation of a monostable metamaterial chain away from a heat source (MP4)

Actuation of a tristable metamaterial chain away from a heat source (MP4)

Pneumatic actuation of a tristable metamaterial from the closed state (MP4)

Additional data and figures on material fabrication, characterization, and numerical modeling (PDF)

AUTHOR INFORMATION

Corresponding Author

Jordan R. Raney – Department of Mechanical Engineering and Applied Mechanics, University of Pennsylvania, Philadelphia, Pennsylvania 19104, United States;
orcid.org/0000-0001-5329-9980; Email: raney@seas.upenn.edu

Authors

Lucia M. Korpas – Department of Mechanical Engineering and Applied Mechanics, University of Pennsylvania, Philadelphia, Pennsylvania 19104, United States

Rui Yin – Department of Mechanical Engineering and Applied Mechanics, University of Pennsylvania, Philadelphia, Pennsylvania 19104, United States

Hiromi Yasuda – Department of Mechanical Engineering and Applied Mechanics, University of Pennsylvania, Philadelphia, Pennsylvania 19104, United States

Complete contact information is available at: <https://pubs.acs.org/doi/10.1021/acsami.1c07327>

Author Contributions

[†]L.M.K. and R.Y. contributed equally to this work.

Notes

The authors declare no competing financial interest.

ACKNOWLEDGMENTS

The authors gratefully acknowledge support from the Air Force Office of Scientific Research award number FA9550-19-1-0285 and DARPA YFA award number W911NF2010278. The authors also thank Peter Szczesniak and the staff of the University of Pennsylvania Precision Machining Laboratory for assistance with fabrication of test fixtures.

REFERENCES

- (1) Zhao, Z.; Wang, K.; Zhang, L.; Wang, L.-C.; Song, W.-L.; Fang, D. Stiff Reconfigurable Polygons for Smart Connectors and Deployable Structures. *Int. J. Mech. Sci.* **2019**, *161–162*, No. 105052.
- (2) Faber, J. A.; Arrieta, A. F.; Studart, A. R. Bioinspired Spring Origami. *Science* **2018**, *359*, 1386–1391.
- (3) Filipov, E. T.; Tachi, T.; Paulino, G. H. Origami Tubes Assembled into Stiff, Yet Reconfigurable Structures and Metamaterials. *Proc. Natl. Acad. Sci. U.S.A.* **2015**, *112*, 12321–12326.
- (4) Overvelde, J. T. B.; de Jong, T. A.; Shevchenko, Y.; Becerra, S. A.; Whitesides, G. M.; Weaver, J. C.; Hoberman, C.; Bertoldi, K. A.

Three-dimensional Actuated Origami-inspired Transformable Meta-material with Multiple Degrees of Freedom. *Nat. Commun.* **2016**, *7*, No. 10929.

(5) Bilal, O. R.; Foehr, A.; Daraio, C. Reprogrammable Phononic Metasurfaces. *Adv. Mater.* **2017**, *29*, No. 1700628.

(6) Khajetourian, R.; Kochmann, D. M. Phase Transformations in Substrate-Free Dissipative Multistable Metamaterials. *Extreme Mech. Lett.* **2020**, *37*, No. 100700.

(7) Deng, B.; Chen, L.; Wei, D.; Tournat, V.; Bertoldi, K. Pulse-Driven Robot: Motion via Solitary Waves. *Sci. Adv.* **2020**, *6*, No. eaaz1166.

(8) Tang, Y.; Li, Y.; Hong, Y.; Yang, S.; Yin, J. Programmable Active Kirigami Metasheets with More Freedom of Actuation. *Proc. Natl. Acad. Sci. U.S.A.* **2019**, *116*, 26407–26413.

(9) Tolley, M. T.; Shepherd, R. F.; Mosadegh, B.; Galloway, K. C.; Wehner, M.; Karpelson, M.; Wood, R. J.; Whitesides, G. M. A Resilient, Untethered Soft Robot. *Soft Rob.* **2014**, *1*, 213–223.

(10) Felton, S.; Tolley, M.; Demaine, E.; Rus, D.; Wood, R. Applied Origami. A Method for Building Self-folding Machines. *Science* **2014**, *345*, 644–646.

(11) Jin, L.; Khajetourian, R.; Mueller, J.; Rafsanjani, A.; Tournat, V.; Bertoldi, K.; Kochmann, D. M. Guided Transition Waves in Multistable Mechanical Metamaterials. *Proc. Natl. Acad. Sci. U.S.A.* **2020**, *117*, 2319–2325.

(12) Yasuda, H.; Korpas, L. M.; Raney, J. R. Transition Waves and Formation of Domain Walls in Multistable Mechanical Metamaterials. *Phys. Rev. Appl.* **2020**, *13*, No. 054067.

(13) Zareei, A.; Deng, B.; Bertoldi, K. Harnessing Transition Waves to Realize Deployable Structures. *Proc. Natl. Acad. Sci. U.S.A.* **2020**, *117*, 4015–4020.

(14) Raney, J. R.; Nadkarni, N.; Daraio, C.; Kochmann, D. M.; Lewis, J. A.; Bertoldi, K. Stable Propagation of Mechanical Signals in Soft Media Using Stored Elastic Energy. *Proc. Natl. Acad. Sci. U.S.A.* **2016**, *113*, 9722–9727.

(15) Ion, A.; Wall, L.; Kovacs, R.; Baudisch, P. In *Digital Mechanical Metamaterials*, Proceedings of the 2017 CHI Conference on Human Factors in Computing Systems, New York, NY, USA, 2017; pp 977–988.

(16) Yasuda, H.; Tachi, T.; Lee, M.; Yang, J. Origami-Based Tunable Truss Structures for Non-volatile Mechanical Memory Operation. *Nat. Commun.* **2017**, *8*, No. 962.

(17) Faber, J. A.; Udani, J. P.; Riley, K. S.; Studart, A. R.; Arrieta, A. F. Dome-Patterned Metamaterial Sheets. *Adv. Sci.* **2020**, *7*, No. 2001955.

(18) Wang, Y.; Dang, A.; Zhang, Z.; Yin, R.; Gao, Y.; Feng, L.; Yang, S. Repeatable and Reprogrammable Shape Morphing from Photo-responsive Gold Nanorod/Liquid Crystal Elastomers. *Adv. Mater.* **2020**, *32*, No. 2004270.

(19) He, Q.; Wang, Z.; Wang, Y.; Song, Z.; Cai, S. Recyclable and Self-Repairable Fluid-Driven Liquid Crystal Elastomer Actuator. *ACS Appl. Mater. Interfaces* **2020**, *12*, 35464–35474.

(20) He, Q.; Wang, Z.; Wang, Y.; Minori, A.; Tolley, M. T.; Cai, S. Electrically Controlled Liquid Crystal Elastomer-based Soft Tubular Actuator with Multimodal Actuation. *Sci. Adv.* **2019**, *5*, No. eaax5746.

(21) Ambulo, C. P.; Burroughs, J. J.; Boothby, J. M.; Kim, H.; Shankar, M. R.; Ware, T. H. Four-dimensional Printing of Liquid Crystal Elastomers. *ACS Appl. Mater. Interfaces* **2017**, *9*, 37332–37339.

(22) Kotikian, A.; Truby, R. L.; Boley, J. W.; White, T. J.; Lewis, J. A. 3D Printing of Liquid Crystal Elastomeric Actuators with Spatially Programmed Nematic Order. *Adv. Mater.* **2018**, *30*, No. 1706164.

(23) Saed, M. O.; Ambulo, C. P.; Kim, H.; De, R.; Raval, V.; Searles, K.; Siddiqui, D. A.; Cue, J. M. O.; Stefan, M. C.; Shankar, M. R.; Ware, T. H. Molecularly-Engineered, 4D-Printed Liquid Crystal Elastomer Actuators. *Adv. Funct. Mater.* **2019**, *29*, No. 1806412.

(24) Barnes, M.; Sajadi, S. M.; Parekh, S.; Rahman, M. M.; Ajayan, P. M.; Verduzco, R. Reactive 3D Printing of Shape-Programmable Liquid Crystal Elastomer Actuators. *ACS Appl. Mater. Interfaces* **2020**, *12*, 28692–28699.

(25) Loukaides, E. G.; Smoukov, S. K.; Seffen, K. A. Magnetic Actuation and Transition Shapes of a Bistable Spherical Cap. *Int. J. Smart Nano Mater.* **2014**, *5*, 270–282.

(26) Crivaro, A.; Sheridan, R.; Frecker, M.; Simpson, T. W.; Von Lockette, P. Bistable Compliant Mechanism Using Magneto Active Elastomer Actuation. *J. Intell. Mater. Syst. Struct.* **2016**, *27*, 2049–2061.

(27) López-Valdeolivas, M.; Liu, D.; Broer, D. J.; Sánchez-Somolinos, C. 4D Printed Actuators with Soft-Robotic Functions. *Macromol. Rapid Commun.* **2018**, *39*, No. 1700710.

(28) Kotikian, A.; McMahan, C.; Davidson, E. C.; Muhammad, J. M.; Weeks, R. D.; Daraio, C.; Lewis, J. A. Untethered Soft Robotic Matter with Passive Control of Shape Morphing and Propulsion. *Sci. Rob.* **2019**, *4*, No. eaax7044.

(29) Minori, A. F.; He, Q.; Glick, P. E.; Adibnazari, I.; Stopol, A.; Cai, S.; Tolley, M. T. Reversible Actuation for Self-Folding Modular Machines Using Liquid Crystal Elastomer. *Smart Mater. Struct.* **2020**, *29*, No. 105003.

(30) Chen, T.; Bilal, O. R.; Shea, K.; Daraio, C. Harnessing Bistability for Directional Propulsion of Untethered, Soft Robots. *Proc. Natl. Acad. Sci. U.S.A.* **2018**, *115*, 5698–5702.

(31) Novelino, L. S.; Ze, Q.; Wu, S.; Paulino, G. H.; Zhao, R. Untethered Control of Functional Origami Microrobots with Distributed Actuation. *Proc. Natl. Acad. Sci. U.S.A.* **2020**, *117*, 24096–24101.

(32) Jiang, Y.; Korpas, L. M.; Raney, J. R. Bifurcation-Based Embodied Logic and Autonomous Actuation. *Nat. Commun.* **2019**, *10*, No. 128.

(33) Hao, X. P.; Xu, Z.; Li, C. Y.; Hong, W.; Zheng, Q.; Wu, Z. L. Kirigami-Design-Enabled Hydrogel Multimorphs with Application as a Multistate Switch. *Adv. Mater.* **2020**, *32*, No. 2000781.

(34) Treml, B.; Gillman, A.; Buskohl, P.; Vaia, R. Origami Mechanologic. *Proc. Natl. Acad. Sci. U.S.A.* **2018**, *115*, 6916–6921.

(35) Chen, T.; Zhanga, X.; Yana, X.; Zhang, B.; Jiang, J.; Zhang, S.; Guo, C.; Huang, D.; Qi, M. In *Phase Transforming Auxetic Material with Embedding Magnets*, Proceedings of SPIE 10968, Behavior and Mechanics of Multifunctional Materials XIII, 2019; p 109680W.

(36) Grima, J. N.; Caruana-Gauci, R.; Dudek, M. R.; Wojciechowski, K. W.; Gatt, R. Smart Metamaterials with Tunable Auxetic and Other Properties. *Smart Mater. Struct.* **2013**, *22*, No. 084016.

(37) Tipton, C. R.; Han, E.; Mullin, T. Magneto-Elastic Buckling of a Soft Cellular Solid. *Soft Matter* **2012**, *8*, 6880–6883.

(38) Cui, Y.; Wang, C.; Sim, K.; Chen, J.; Li, Y.; Xing, Y.; Yu, C.; Song, J. A Simple Analytical Thermo-mechanical Model for Liquid Crystal Elastomer Bilayer Structures. *AIP Adv.* **2018**, *8*, No. 025215.

(39) Agrawal, A.; Yun, T.; Pesek, S. L.; Chapman, W. G.; Verduzco, R. Shape-Responsive Liquid Crystal Elastomer Bilayers. *Soft Matter* **2014**, *10*, 1411–1415.

(40) Boothby, J. M.; Ware, T. H. Dual-Responsive, Shape-Switching Bilayers Enabled by Liquid Crystal Elastomers. *Soft Matter* **2017**, *13*, 4349–4356.

(41) Timoshenko, S. Analysis of Bi-metal Thermostats. *J. Opt. Soc. Am.* **1925**, 233–255.